JOURNAL OF GEOPHYSICAL RESEARCH, VOL. 110, C06014, doi:10.1029/2003JC001814, 2005

Estimating hydrodynamic roughness in a wave-dominated environment with a high-resolution acoustic Doppler profiler

Jessica R. Lacy,[1] Christopher R. Sherwood,[2] Douglas J. Wilson,[3] Thomas A. Chisholm,[4] and Guy R. Gelfenbaum[5]

Received 7 February 2003; revised 13 February 2005; accepted 24 March 2005; published 30 June 2005.

[1] Hydrodynamic roughness is a critical parameter for characterizing bottom drag in boundary layers, and it varies both spatially and temporally due to variation in grain size, bedforms, and saltating sediment. In this paper we investigate temporal variability in hydrodynamic roughness using velocity profiles in the bottom boundary layer measured with a high-resolution acoustic Doppler profiler (PCADP). The data were collected on the ebb-tidal delta off Grays Harbor, Washington, in a mean water depth of 9 m. Significant wave height ranged from 0.5 to 3 m. Bottom roughness has rarely been determined from hydrodynamic measurements under conditions such as these, where energetic waves and medium-to-fine sand produce small bedforms. Friction velocity due to current u_{*c} and apparent bottom roughness z_{0a} were determined from the PCADP burst mean velocity profiles using the law of the wall. Bottom roughness k_B was estimated by applying the Grant-Madsen model for wave-current interaction iteratively until the model u_{*c} converged with values determined from the data. The resulting k_B values ranged over 3 orders of magnitude (10^{-1} to 10^{-4} m) and varied inversely with wave orbital diameter. This range of k_B influences predicted bottom shear stress considerably, suggesting that the use of time-varying bottom roughness could significantly improve the accuracy of sediment transport models. Bedform height was estimated from k_B and is consistent with both ripple heights predicted by empirical models and bedforms in sonar images collected during the experiment.

Citation: Lacy, J. R., C. R. Sherwood, D. J. Wilson, T. A. Chisholm, and G. R. Gelfenbaum (2005), Estimating hydrodynamic roughness in a wave-dominated environment with a high-resolution acoustic Doppler profiler, *J. Geophys. Res.*, *110*, C06014, doi:10.1029/2003JC001814.

1. Introduction

[2] Bottom shear stress and hydrodynamic roughness are essential parameters in determining sediment resuspension and transport, but they are difficult to measure directly. In a fully developed unidirectional flow, friction velocity (which is directly related to bottom shear stress) and hydrodynamic roughness can be determined from velocity profiles in the bottom boundary layer, using the law of the wall. In contrast, in a combined wave-current flow, the thin wave boundary layer interacts directly with the physical bottom roughness, and the near-bed turbulence generated by the waves influences the mean velocity profile in a manner analogous to physical roughness (known as apparent roughness). Bottom shear stress and bottom roughness cannot be estimated directly from measurements made outside the wave boundary layer, so models of wave-current interaction have been developed to estimate bottom shear stress [e.g., *Jonsson*, 1966; *Smith*, 1977; *Grant and Madsen*, 1979; *Styles and Glenn*, 2000]. These models require an estimate of physical bottom roughness k_B as an input.

[3] The roughness length scale k_B is difficult to estimate and changes over time, because it is influenced by grain size, bedform geometry, and near-bed sediment transport. In a steady turbulent flow over a sandy bed, bottom roughness k_B is a combination of skin friction associated with grain roughness and form drag caused by ripples, dunes, or biogenic features. In addition, when sediment is mobile, momentum is extracted from the flow and transferred to saltating grains, effectively increasing the bottom drag. The contribution of these three factors is generally treated as additive, so that the overall length scale for bed roughness is $k_B = k_N + k_{ST} + k_{BF}$, where k_N is the Nikuradse grain roughness, k_{ST} is the saltation roughness, and k_{BF} is the bedform roughness [*Smith*, 1977; *Cacchione and Drake*, 1990].

[1]U.S. Geological Survey, Santa Cruz, California, USA.
[2]U.S. Geological Survey, Woods Hole, Massachusetts, USA.
[3]Imagenex Technology Corporation, Port Coquitlam, British Columbia, Canada.
[4]Department of Environmental Science and Engineering, Oregon Graduate Institute, Beaverton, Oregon, USA.
[5]U.S. Geological Survey, Menlo Park, California, USA.

0148-0227/05/2003JC001814$09.00

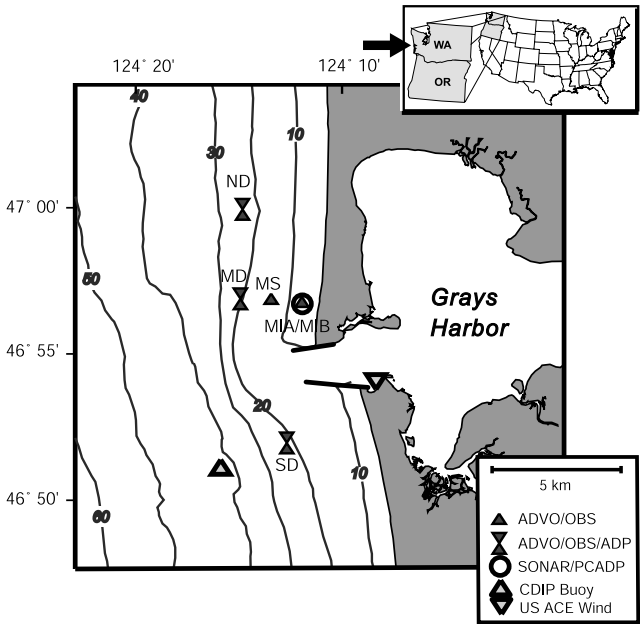

Figure 1. Chart of region offshore of Grays Harbor, Washington. Contour interval is 10 m. Data discussed in this paper were collected at sites MIA and MIB.

[4] Methods for estimating k_B by assessing the contribution of these three components have been proposed by *Grant and Madsen* [1982], *Nielsen* [1992], *Wikramanayake and Madsen* [1991], *Xu and Wright* [1995], *Li and Amos* [1998], and *Styles and Glenn* [2002], among others, based on both laboratory and field data. The influence of the components of k_B on the bottom boundary layer has been studied primarily in the laboratory. However, most laboratory facilities cannot replicate the complexity of field environments, where currents typically flow alongshore and are often almost orthogonal to the direction of wave propagation.

[5] Another approach to estimating k_B, which we follow in this paper, is to rely on hydrodynamic measurements. In this approach, k_B is determined from its influence on friction velocity and the velocity profile in the current boundary layer. We estimate the length scale of physical bottom roughness k_B by using the Grant-Madsen model for wave-current interaction [*Grant and Madsen*, 1979; *Madsen*, 1994] in an inverse mode. The inverse method is applied to a data set of more than 800 mean velocity profiles collected over 2 months with a pulse-coherent acoustic Doppler profiler (PCADP). Friction velocity due to currents u_{*c} and apparent bottom roughness z_{0a} are estimated from the profiles based on the law of the wall, and are used as inputs to the inverse model. The estimates of bottom roughness, denoted $\hat{k}_B$, vary inversely with wave orbital diameter and the range of variation is great enough to significantly influence bottom shear stress. Bedform heights are estimated from the $\hat{k}_B$ and compared to those predicted by empirical formulae and to bedform categories observed in sonar images.

[6] Previous estimates of physical bottom roughness through inverse use of a wave-current model have been presented by *Madsen et al.* [1993], *Xu and Wright* [1995], and *Styles and Glenn* [2002]. *Madsen et al.* [1993] and *Xu and Wright* [1995] estimated bottom roughness at only a few points in time due to limitations in the measurements of velocity profiles. In our study, the PCADP data allowed calculation of hundreds of values of u_{*c} so that variation of k_B over time can be examined. The study site was characterized by energetic waves, fine sand, and small ripples, contrasting with the lower-energy conditions and larger orbital ripples investigated by *Styles and Glenn* [2002] and *Traykovski et al.* [1999]. *Trembanis et al.* [2004] also estimate bottom roughness from hydrodynamic measurements. They determine u_{*c} from high-frequency velocity measurements at a single point by the inertial dissipation method, and use u_{*c} to estimate the wave friction factor, which has been empirically related to bottom roughness.

2. Field Program

2.1. Study Site

[7] Sediment transport data were collected off the coast of southwest Washington outside of Grays Harbor during the summer of 2001, in a study linking seasonal changes in sediment transport around the ebb-tidal delta off Grays Harbor to erosion and accretion on the adjacent coast [*Landerman et al.*, 2005] (Figure 1). The Washington coast is characterized by rough wave conditions and large tides, with tidal range exceeding 3 m during spring tides. In summer, significant wave heights measured at the CDIP buoy (Figure 1) are typically 1–2 m, and reach 4 m during periods of strong southerly winds. This paper describes data from the inner shelf at a site with a mean depth of 9 m (MIA and MIB, Figure 1). Bed sediments are well-sorted fine sand comprised of quartz, feldspar, and metamorphic and volcanic rock fragments, typical of the coarser fraction of material delivered by the Columbia River. Sediment in grab samples from MIA was well-sorted fine sand with median grain size D = 0.15 mm (D_{85} = 0.18 mm).

2.2. Data Collection

[8] Two instrumented tripods were deployed to measure currents, waves, and suspended sediment in the bottom boundary layer, and to record sonar images of bedforms. The tripods were deployed 4 May 2001 and recovered

Table 1. PCADP Sampling Parameters[a]

Parameter	Deployment 1	Deployment 2
No. cells	8	8
Cell size	10.8 cm	9.4 cm
Blanking distance	10 cm	10 cm
Profiling interval	1 s	1 s
Burst interval	3600 s	3600 s
Profiles per burst	1200	1200
Profiling lag	1.09 m	0.97 m
Resolution lag	0.49 m	0.49 m
Res. blanking distance	0.24 m	0.24 m
Maximum horizontal velocity	±64 cm/s	±72 cm/s
Maximum horizontal velocity with ambiguity error resolution	±143 cm/s	±143 cm/s
Pings per profile	9–10	13–15

[a]Distances are vertical rather than along beam. Units are those used in PCADP commands. Number of significant figures is that provided in PCADP control file.

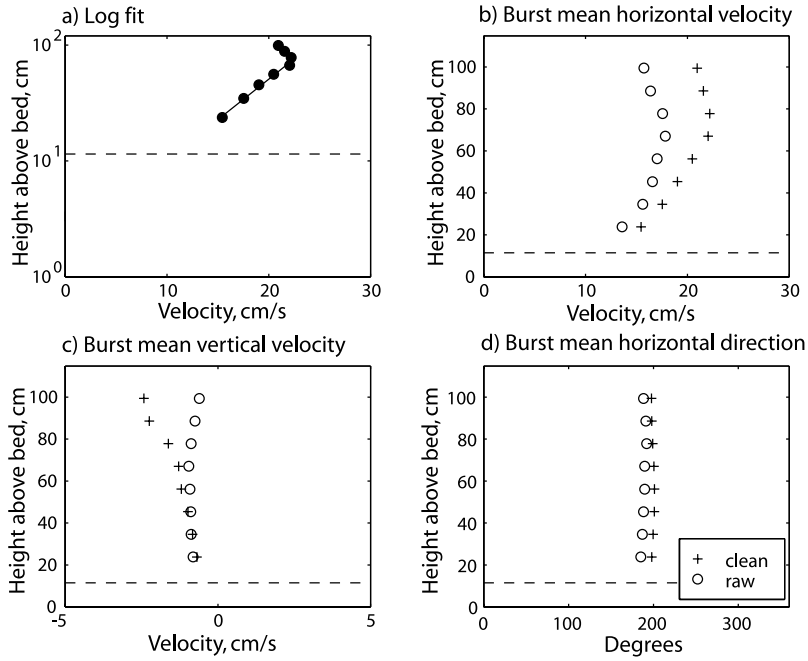

Figure 2. Example of burst mean profile measured by PCADP before (circles) and after (pluses) ambiguity error correction. (a) Burst mean (corrected) horizontal velocity versus logarithm of height above bed, with logarithmic fit to bottom 5 bins. Profiles of (b) burst mean horizontal velocity, (c) burst mean vertical velocity, and (d) current direction. Dashed line shows level below which reflection from the bottom is expected to interfere with velocity measurement. Velocities from top three bins were not used in logarithmic fits.

11 July 2001, with one turn-around 6–8 June to change batteries, recover data, and clean sensors. At station MIA a 1.5 MHz Sontek PCADP was mounted on the tripod looking downward from a height of 130 cm, to measure velocity profiles in the bottom meter above the bed. The PCADP measured velocity in eight 10-cm (nominal) cells, at 1 Hz. Other sampling parameters for the PCADP are shown in Table 1. A Paros Scientific Digiquartz pressure sensor connected to the PCADP measured pressure at 1 Hz. The PCADP sampled for 20-min bursts every hour. The first 118 of the 810 PCADP bursts from the second deployment had persistently low correlations (<25%) in cells 1–3, indicating poor data quality, and were not included in our analyses. Two Sontek Field acoustic Doppler velocimeters (ADVF), an Aquatec acoustic backscatter sensor (ABS), and six D&A Instruments optical backscatter sensors (OBS) were also mounted on the MIA tripod. The data collected by these instruments are not discussed in this paper.

[9] On a second tripod (station MIB), located approximately 50 m north from MIA, a Sontek Ocean acoustic Doppler velocimeter (ADVO) measured velocity and a sonar system collected images of the bottom [*Hay and Wilson*, 1994]. An Imagenex model 858 controlled two model 855 sonar heads operating at 2.25 MHz. One of the sonar heads emitted a fan beam and rotated 360° about a vertical axis, producing a plan view image (effective diameter ~5 m) of the seafloor. The other head emitted a narrow conical bean and rotated 360° about a horizontal axis, producing a profile of the bed. The sonars collected images every 2 hours. Each scan took 45 s, and images were constructed from averages of one or two scans. Sonar images were recorded only for about 2 weeks during each deployment (11–26 May and 8–23 June) owing to limitations of the data logger.

[10] Bed elevation was determined from the profiling data by comparing low-pass filtered returns to the maximum return of each ping, working inward from below the bottom. The elevation of the bed was defined as the location of the first return exceeding 75% of the maximum value. The bottom elevations, which had a horizontal spacing ranging from about 1.6 cm directly under the transducer to about 4.3 cm at 2 m from the transducer, were interpolated to 400 elevations spaced 1 cm apart, and spikes were removed. The error in determining bed elevation from the profiles was ±1 cm, too great to resolve the amplitude of the small ripples that were present during the experiment.

2.3. Accuracy of the PCADP

[11] Because the PCADP has not been extensively field tested in wave-dominated environments, we used the ADVF velocities to check its accuracy. The results of our evaluation are reported by *Lacy and Sherwood* [2004] and are summarized below. Ambiguity errors were corrected as described by *Lacy and Sherwood* [2004]. Errors in instantaneous velocity, burst mean speed, and bottom orbital velocity were determined for PCADP cell 5 by comparing them to values measured at the same elevation by the ADVF. The average error in burst mean speed was −0.4 cm/s (s.d. 0.8). The average error in the bottom orbital velocity u_{br} calculated by the PCADP was

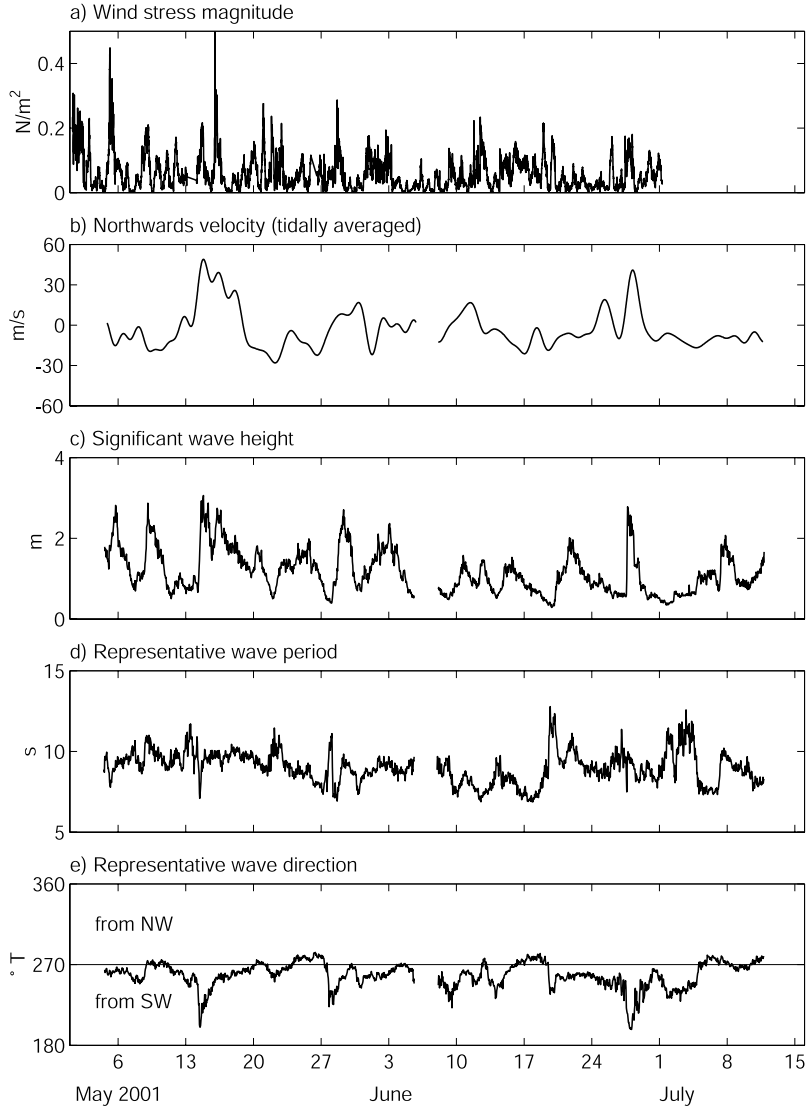

Figure 3. Conditions during the experiment. (a) Wind stress measured at Westport, Washington. (b) Depth-averaged northward velocity measured at Station MD (see Figure 1), low-pass filtered to remove tides. (c) Significant wave height. (d) Representative wave period. (e) Wave direction at MIA.

0.7 cm/s (s.d. 1.3), indicating a slight positive bias. Error in u_{br} increased significantly for bursts with $u_{br} > 70$ cm/s because these bursts included instantaneous velocities greater than the threshold for ambiguity errors for the PCADP resolution pulse, which was 120 cm/s. We retained these bursts in our analysis because the error in u_{br} was <10%.

[12] The velocity profiles measured by the PCADP typically follow the expected logarithmic bottom boundary layer profile in the five bottom bins (farthest from the transducers), but in the cells closest to the transducers mean speeds are lower than expected (Figure 2). Vertical velocities are frequently higher in magnitude than is reasonable, with increasing magnitude closer to the transducers. The poor data quality in the cells close to the transducers is created by near-field acoustic effects [*Lacy and Sherwood*, 2004]. The negative vertical velocities also suggest the possibility of flow disturbance by the tripod. Data from the top three cells were not used in our analysis unless they were consistent with the logarithmic profile defined by the bottom five cells.

2.4. Conditions During the Experiment

[13] Winds, waves, and currents shifted from spring to summer conditions over the course of the experiment (Figure 3). Wind stress and wave height decreased as the summer progressed, and currents were predominantly southwards. There were several periods of strong winds from the south that produced wave heights up to 3 m, northward currents, and brief veering of the wave propagation direction toward the north. The grain roughness Shields parameter [*Nielsen*, 1992] exceeded the threshold for sediment motion ($\theta_c = 0.05$) throughout the experiment.

[14] Near-bed currents up to 0.40 m/s and bottom orbital velocities up to 1 m/s occurred during the experiment (Figure 4). Wave velocities dominated currents: the median of the ratio of mean current to representative orbital velocity 0.5 m above the bed was 0.23 (Figure 4c). The angle

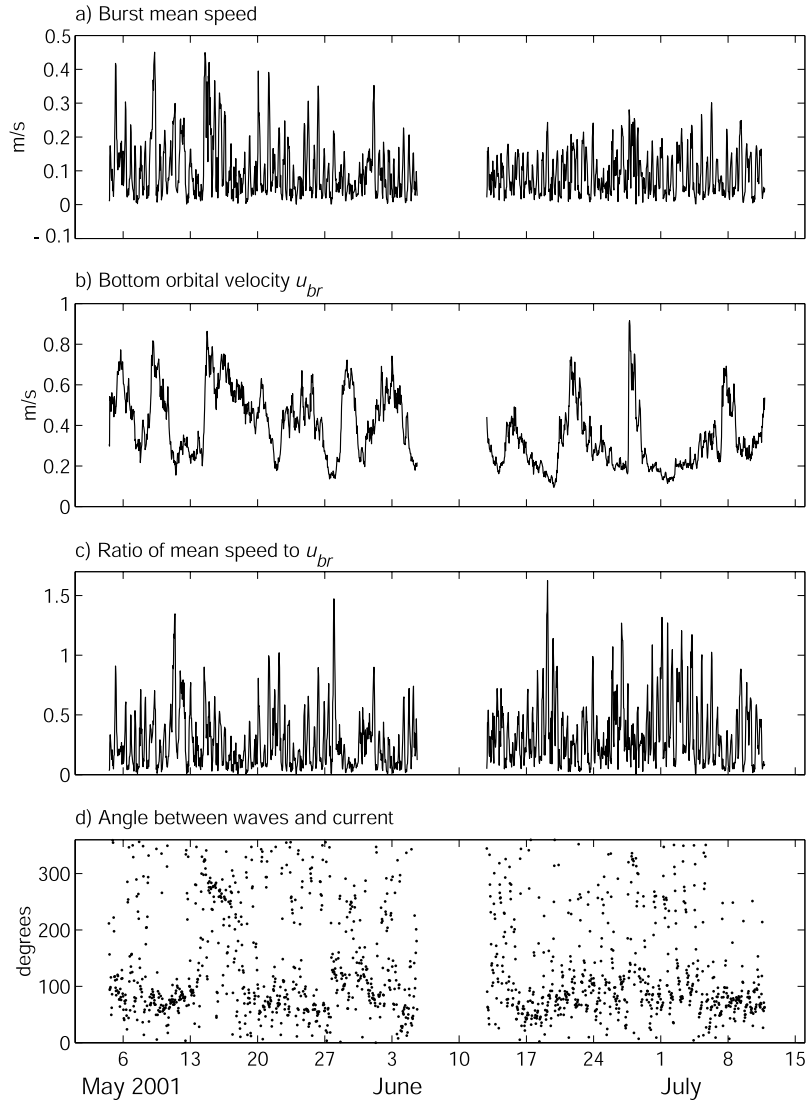

Figure 4. (a) Burst mean speed, (b) bottom orbital velocity, (c) ratio of burst mean speed to bottom orbital velocity, and (d) angle between current and wave propagation directions.

between the current and the propagation of waves was typically close to 90° (Figure 4d).

3. Methodology

3.1. Wave-current Boundary Layers

[15] The velocity profile in the bottom boundary layer in unidirectional steady flows is governed by the law of the wall,

$$u(z) = u_* \frac{1}{\kappa} \ln\left(\frac{z}{z_0}\right), \tag{1}$$

where u is horizontal velocity, u_* is friction velocity, $\kappa = 0.41$ is the Von Kármán constant, z is the height above the bed, and z_0 is the hydrodynamic roughness. Friction velocity u_* and z_0 can be determined by fitting a measured velocity profile to this equation.

[16] The boundary layer created by steady currents is fully developed and thus typically extends for meters above the bed, or to the height of a change in density. Wave boundary layers, on the other hand, have only a few seconds to develop and thus are much thinner, typically less than 10 cm. In a combined wave and current flow, the influence of the wave boundary layer on the current boundary layer can be modeled as an increase in roughness [*Grant and Madsen*, 1979]. Mean velocities above the wave boundary layer are logarithmically distributed with respect to depth; however, the y-intercept occurs at a higher elevation when waves are present. Close to the bed, currents are reduced by the increased turbulence associated with the wave boundary layer. The influence of waves on the mean flow can be characterized as an increase in eddy viscosity ν_t within the wave boundary layer,

$$\nu_t = \begin{cases} \kappa u_{*cw} z & z < \delta_w \\ \kappa u_{*c} z & z > \delta_w, \end{cases} \tag{2}$$

where δ_w is the height of the wave boundary layer, u_{*c} denotes the friction velocity due to the current, and u_{*cw}

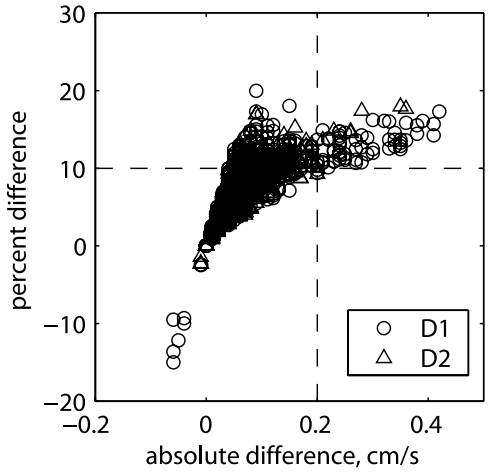

Figure 5. Influence of stratification on u_{*c} as predicted by the Wiberg model. Circles denote bursts from deployment 1, and triangles are bursts from deployment 2. Bottom roughness and bedform heights were not estimated if the predicted difference in u_{*c} fell above the horizontal dotted line and to the right of the vertical dotted line. Influence of stratification on unstratified $u_{*c} < 0.4$ cm/s not included in plot.

denotes the maximum friction velocity at the bed due to the combination of the waves and current. Although instantaneous bottom shear stress and turbulent mixing vary over the wave period, this expression for time-invariant eddy viscosity has been used successfully to characterize the influence of waves on the mean velocity profile in a number of models of wave-current interaction. The expressions for the mean current above and within the wave boundary layer following from equation (2) are

$$u(z) = \begin{cases} \dfrac{u_{*c}^2}{\kappa\, u_{*cw}} \ln\left(\dfrac{z}{z_0}\right) & z < \delta_w \\ \dfrac{u_{*c}}{\kappa} \ln\left(\dfrac{z}{z_{0a}}\right) & z > \delta_w, \end{cases} \tag{3}$$

where z_{0a} is known as the apparent roughness.

[17] The Grant-Madsen model (GM) for wave-current interaction [*Grant and Madsen*, 1979; *Madsen*, 1994] is an eddy-viscosity model that uses mean and bottom orbital velocities at a reference depth, the angle between waves and currents, and the bottom roughness $k_B = 30\, z_0$ to predict u_{*c}, z_{0a}, u_{*cw}, and bottom shear stress $\tau_b = \rho u_{*cw}^2$. Maximum wave-current friction velocity at the bed u_{*cw} is determined from u_{br} using a wave friction factor, modified to account for the current. Friction velocity due to current u_{*c} and z_{0a} are determined by requiring that the function $u(z)$ defined by equation (3) be continuous at $z = \delta_w$, using the input value of z_0 and estimating the height of the wave boundary layer δ_w from u_{*cw} and the wave period.

[18] For input to GM, representative bottom orbital velocity was calculated as

$$u_{br} = \sqrt{2 \int (S_{uu}(\omega) + S_{vv}(\omega)) d\omega}, \tag{4}$$

where S_{uu} and S_{vv} are spectra of the horizontal components of near-bottom velocity as a function of wave frequency ω [*Madsen*, 1994], and is referred to here as bottom orbital velocity or u_{br}. Wave orbital diameter was calculated as $d_o = u_{br} \cdot T/\pi$, where T is the representative wave period.

[19] Laboratory and field studies have identified a number of factors influencing velocity profiles in the wave-current boundary layer that eddy-viscosity models such as GM do not reproduce, including the difference between following and opposing currents, differences caused by the position of the profile relative to bedforms, and temporal variability in eddy viscosity [*Nielsen*, 1992]. Nevertheless, eddy-viscosity models account reasonably well for the nonlinear enhancement of bottom shear stress produced by the combination of waves and current. A comparison of eight models of wave-current interaction showed that the bottom shear stress predicted by GM is consistent with that of the other models and that all the models are generally consistent with the limited available data [*Soulsby et al.*, 1993]. In our data set the angle between waves and current was usually close to 90° (Figure 4d), the angle at which the nonlinear interaction is least and the model predictions are most similar. Although several improvements to GM and other eddy-viscosity models have been developed, including continuous eddy-viscosity formulations and stratification effects [e.g., *Glenn and Grant*, 1987; *Wiberg et al.*, 1994; *Styles and Glenn*, 2000], the models still require bottom roughness k_B as an input parameter. The inability to accurately predict bottom roughness is frequently cited as a significant source of uncertainty in eddy-viscosity models [e.g., *Grant and Madsen*, 1986]. We used the updated 1994 GM formulation [*Madsen*, 1994] in estimating k_B. The relationship of k_B to the eddy-viscosity profile in most eddy-viscosity models is essentially the same as in GM.

3.2. Method for Estimating Bottom Roughness

[20] To estimate k_B we first determined u_{*c} and z_{0a} for each burst by fitting the logarithmic relationship in equation (3) for $z > \delta_w$ to the PCADP burst mean velocity profiles u and measured elevations z. The PCADP measures the distance from the transducer to the bed (accuracy of ±1 cm) with each of the three beams at the beginning of each burst. The mean of the three measurements was used to specify the elevations z of the measured velocities in equation (3). This method accounted for variation in the instrument height due to settling and episodic deposition and erosion during the deployment. The bottom five cells were always used in the logarithmic fits, and cells above them were sequentially added if they increased the correlation coefficient (R^2) between the data and the fitted logarithmic curve. The log fits were used to estimate u_{*c} and z_{0a} for bursts with $R^2 \geq 0.96$ and burst mean speed greater than 5 cm/s at 0.5 m above the bed (cell 5). These criteria were met by 407 out of 769 bursts in deployment 1 and 409 of the 692 bursts in deployment 2. The restriction on R^2 values limits the error in the estimates of u_{*c} and z_{0a}.

[21] Fitting the data to equation (3) requires velocities at a number of discrete depths, rather than the depth-averaged velocities measured by the PCADP, so we assigned the PCADP velocities to the midpoints of the cells. The difference between the depth-averaged velocities

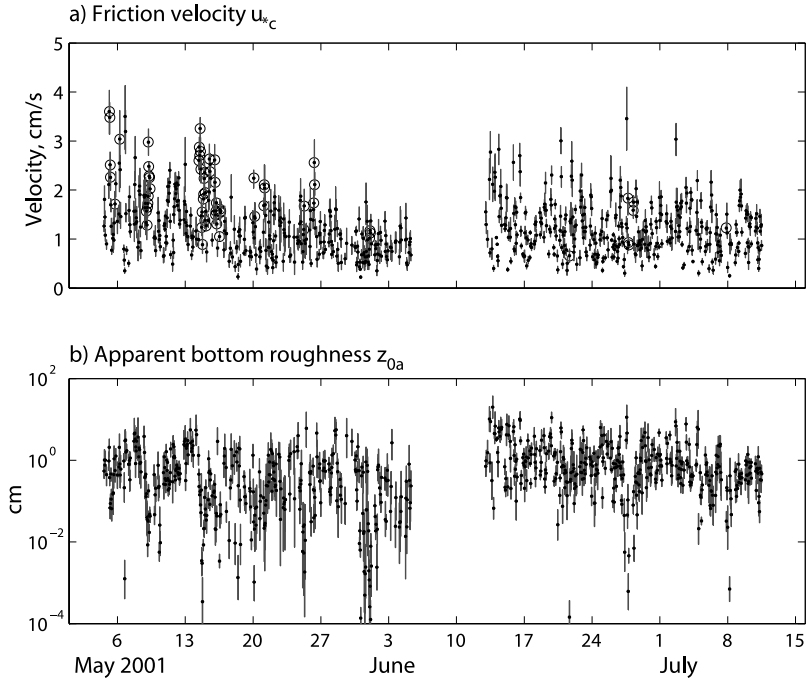

Figure 6. (a) Friction velocity due to current, and (b) apparent bottom roughness. Black points are estimates from log fits, and error bars are 90% confidence limits. Times when Wiberg model indicates that stratification significantly influenced u_{*c} are indicated by circles in Figure 6a.

and the velocities at the midpoints of the cells in a logarithmic profile was negligible for this data set. (For example, in a typical logarithmic profile with u_{*c} = 2 cm/s and z_{0a} = 1 cm, the cell extending from 10 to 20 cm above the bed has a depth-averaged velocity that differs from the velocity at the midpoint by less than 1%. The depth-averaged velocity occurs at 14.72 cm rather than 15 cm above the bed, a difference that is less than the accuracy in measuring the cell elevations.)

[22] Next, the calculated values of u_{*c} were screened for the influence of stratification due to sediment resuspension, which can occur when waves are energetic. Stratification in the bottom boundary layer reduces turbulent mixing and u_{*c}, an effect that is not accounted for by GM. We used the Wiberg model of wave-current interaction [*Wiberg et al.*, 1994] to determine which of the calculated values u_{*c} were likely to be influenced by stratification by comparing model runs that took stratification into account with those that did

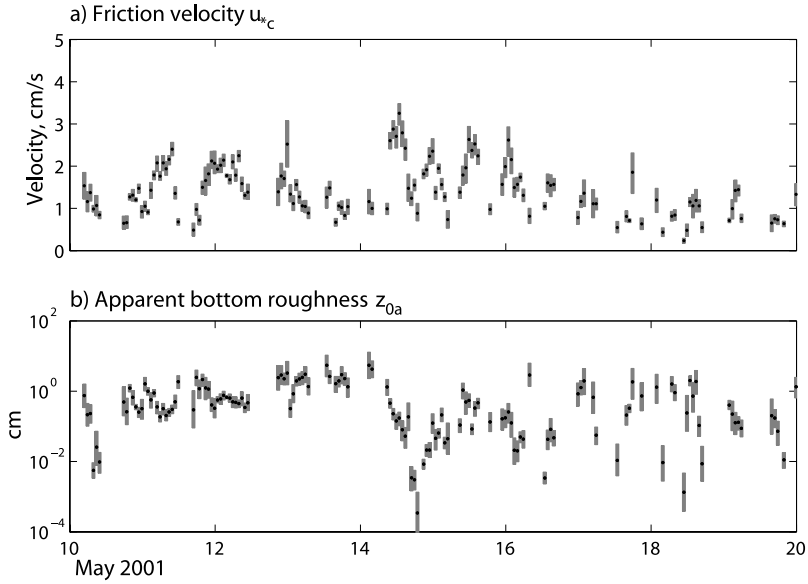

Figure 7. Detail of (a) u_{*c} and (b) apparent bottom roughness from log fits with 90% confidence limits for 10–20 May.

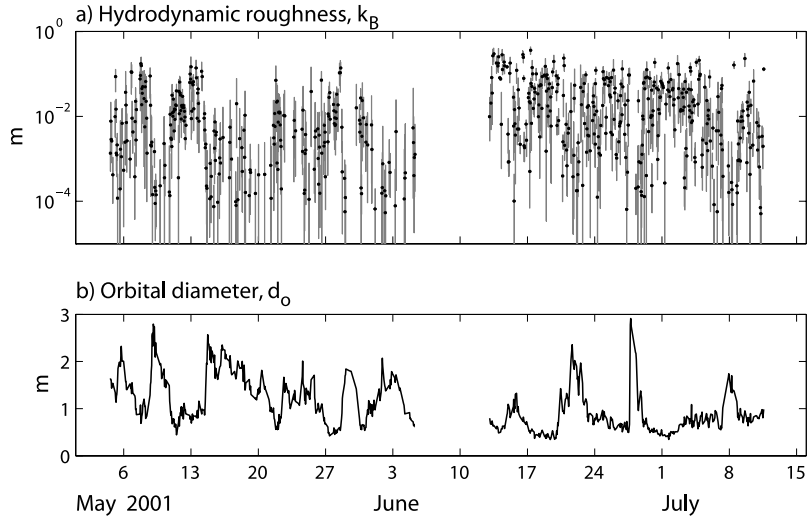

Figure 8. (a) Bottom roughness $\hat{k}_B$ and (b) wave orbital diameter. Error bars for $\hat{k}_B$ are calculated from the upper and lower ends of the confidence interval on u_{*c} in the iterative solution of GM.

not. Bottom roughness was not estimated for bursts in which the predicted influence of stratification on u_{*c} was both greater than 10% and greater than 0.2 cm/s (57 bursts in deployment 1 and 7 bursts in deployment 2) (Figure 5).

[23] Finally, we solved GM iteratively, allowing k_B to vary (between 10^{-5} and 0.4 m) until the predicted u_{*c} converged with the value determined from the log fit. The k_B value producing the expected value of u_{*c} is our estimate of bottom roughness $\hat{k}_B$. The estimate was discarded if it was less than one quarter the grain size or if the predicted u_{*c} did not converge to within 2% of the log-fit value in fewer than 20 iterations.

4. Results

4.1. Estimates of u_{*c} and z_{0a} From Velocity Profiles

[24] Time series of the estimated u_{*c} and z_{0a} are shown in Figure 6, with error bars incorporating the two sources of uncertainty described below. u_{*c} increased during periods of larger waves (9 May, 15–17 May, 28–29 June; see Figure 3c). The section of the time series in Figure 7 shows a tidal signal in the calculated values of u_{*c} as well as a clear response to the event of 15–17 May. Circled values of u_{*c} in Figure 6 indicate that the influence of stratification is predicted by the Wiberg model to be both greater than 10% and greater than 0.2 cm/s. The u_{*c} values shown here incorporate the influence of stratification on near-bed turbulence and the velocity profile, but values predicted by GM would not, so $\hat{k}_B$ was not calculated for these bursts.

[25] Two factors were taken into account in estimating the error in u_{*c} and z_{0a}: uncertainty in the log fits and variation in the distance to bottom measured by the three beams of the PCADP. The error in u_{*c} due to uncertainty in the log fit is calculated as the confidence interval on the slope of a regression line, which can be expressed in terms of R^2 and n [*Gross and Nowell*, 1983]. For R^2 = 0.96 and n = 5, the 90% confidence interval on u_{*c} is ±40%. Errors on estimated u_{*c} are typically lower than ±40% because n and R^2 frequently exceeded the minimum values. The errors due to uncertainty in the log fits for the 816 calculated values of u_{*c} have a median of 8.5%, a ninetieth percentile of 18%, and a maximum of 28%. The error in $\ln(z_{0a})$ is calculated from the error on the y-intercept of a regression. The median error for the 816 calculated values of z_{0a} is $\times\div 1.37$, and the ninetieth percentile is $\times\div 1.9$ (where $a \times\div b$ denotes the range $a \exp[\pm \ln b]$). There are two primary reasons for the large errors in z_{0a}: It is estimated by extrapolating outside the range of depths where velocities are measured, and the

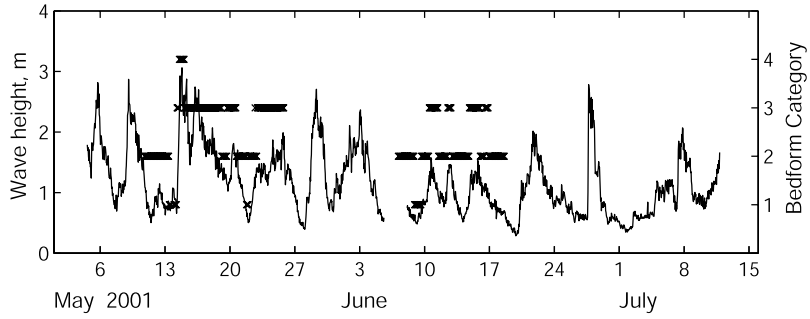

Figure 9. Bedform category from sonar images and significant wave height at MIA: 1 = linear ripples, 2 = irregular ripples, 3 = megaripples, and 4 = flat bed.

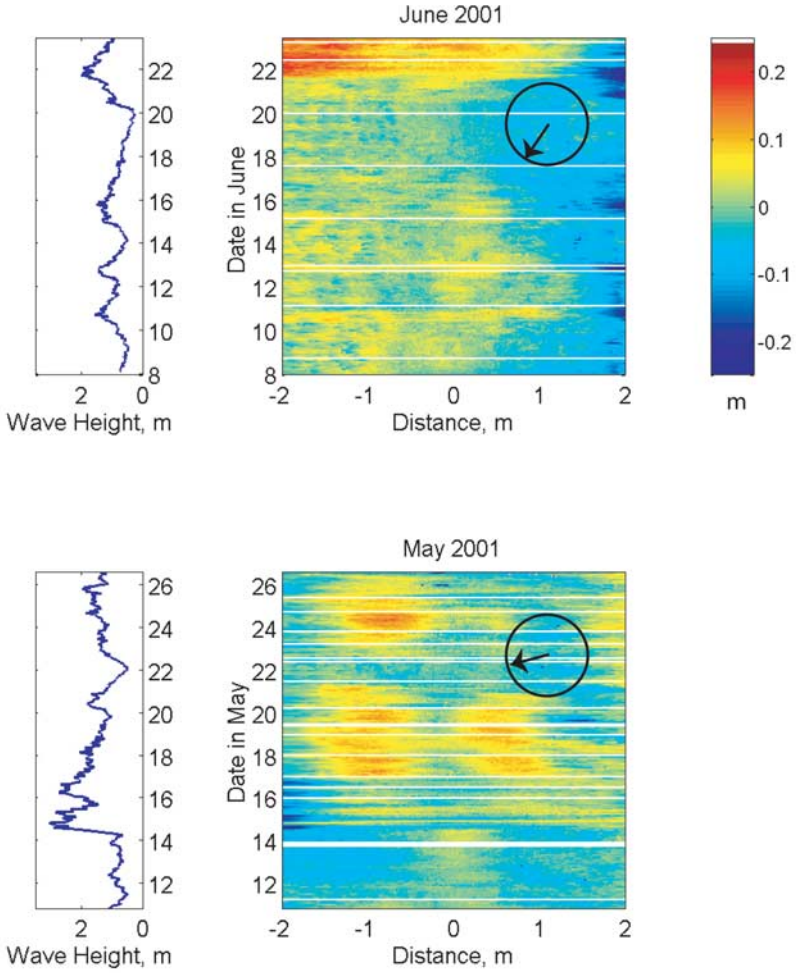

Figure 10. Time series of deviation of bed elevation from the mean, from profiling sonar images. Missing data are indicated by white lines. To correct for settling, 16 cm was added to profiles for 8–10 June. Arrows show offshore direction (270°) relative to horizontal in the bed elevation plots (i.e., May profiles are oriented 280°–100°, and June profiles are oriented 326°–146°).

errors are calculated by taking the exponential of the error in $\ln(z_{0a})$.

[26] The ability of the PCADP to measure the distance to the bottom limits the uncertainty in the heights of the velocity measurements. Nevertheless, some uncertainty is created by variation in the distance to bottom between the three beams caused by bedforms or a sloping bed, as well as by error in the distance measurements. The PCADP uses backscatter from all three beams to calculate three orthogonal components of velocity. When the bed is not flat, velocities from different heights above the bed are combined, particularly in the lowest depth cell where the beams are farthest apart (~0.5 m separation in our experiment). The difference between the minimum ($z_{\min}$) and maximum ($z_{\max}$) of the three distances to bottom measured by the PCADP (after correction for pitch and roll) ranged from 0.9 to 8.5 cm, with a median of 2.9 cm, for the 1461 bursts. To account for this source of error in u_{*c} and z_{0a}, we fit two logarithmic curves to the velocity profile for each burst, one using z-locations based on $z_{\max}$ and the other using elevations based on $z_{\min}$. The combined error from uncertainty in the log fits and irregularity in the bed extends from the upper 90% confidence interval on the fit using $z_{\max}$ to the lower 90% confidence interval using $z_{\min}$. The median of the combined error in u_{*c} is 13%, 90% of the errors are less than 25%, and the maximum error is 45%. The median combined error in z_{0a} is $\times\div 1.75$ (90th percentile: $\times\div 2.9$).

4.2. Inverse Estimate of Bed Roughness

[27] Inverse application of GM produced estimates of bottom roughness k_B for 595 of the 752 bursts with calculated u_{*c} not influenced by stratification (248 of 350 in deployment 1, 347 of 402 in deployment 2). The time series of $\hat{k}_B$ (Figure 8) shows that bed roughness ranged 3 orders of magnitude (from 10^{-4} to 10^{-1} m). The $\hat{k}_B$ was large when waves were smallest (11–14 May, 8–19 June, 30 June to 6 July), and minimum $\hat{k}_B$ occurred during periods of greatest wave energy (9 May, 15–17 May, 22 June, 29 June). The error in $\hat{k}_B$ was estimated by requiring the iterative solution of GM to converge to the upper and lower bounds of the error estimated for u_{*c} for each burst.

4.3. Bedform Categories in Sonar Images

[28] The sonar images show two distinct length scales of variation in bed elevation, with wavelengths of ~1.5 m and ~0.1 m. Both amplitude and wavelength of the large-scale

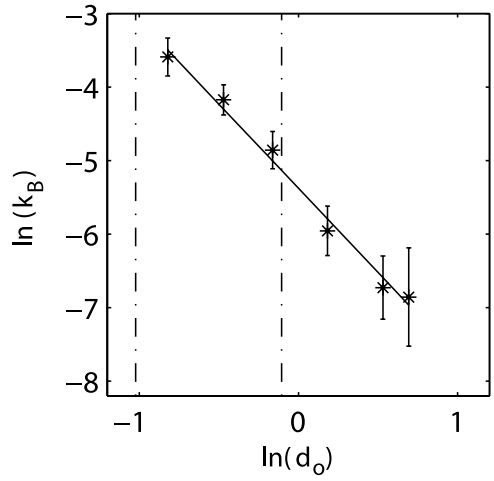

Figure 11. Logarithmic plot of geometric means (with 90% confidence intervals) of estimated roughness k_B versus wave orbital diameter, and least squares fit line. Dash-dotted lines show predicted transitions from orbital to suborbital ripples (left) and from suborbital to anorbital ripples (right).

bedforms can be determined from the profile images, and the wavelengths of the small-scale ripples can be determined from the plan view images. The average wavelength in 27 scans of linear and irregular ripples in May was 9.4 cm (s.d. 1.5 cm).

[29] Bedforms were categorized into four types by examining the sonar images: rippled, irregular, megaripples, and flat bed. This categorization of bedforms that occur in increasingly energetic conditions follows *Clifton* [1976]. Rippled beds were identified by the presence of clearly identifiable linear features in the plan view images. Irregular ripples have similar texture to linear ripples but lack long crests. Megaripples have a smoother and lighter appearance, but with some larger-scale irregularity. Flat bed appears similar to megaripples but lacks large-scale irregularity and has a flat profile. Cross-ripples, which occur in Clifton's categorization between irregular ripples and megaripples, were not distinguishable in the sonar images. Bedforms in the sonar images were categorized without considering other data. The resulting bedform types varied consistently with wave energy (Figure 9). Most of the time the bedforms were irregular ripples or megaripples. Flat bed developed during the most energetic period of the study, on 15 May.

[30] A time series of bed elevation profiles shows large-scale bedforms that were often stable for several days at a time (Figure 10). In particular, during 17–21 May, there were regularly shaped megaripples with wavelengths ~1.5 m and height ~0.1 m. These megaripples occurred after a high-energy period of flat bed, while wave energy was decreasing and wave orbital diameters were 1–2 m (Figure 8b), consistent with the conditions identified by *Li and Amos* [1999] for the occurrence of megaripples in combined wave-current flows. Large-scale bedforms reappeared during 24–26 May and 12–16 June. The depressed bed elevations on the right side of the June subplot of Figure 10 were most likely caused by scour around the tripod leg.

5. Discussion

5.1. Bottom Roughness as a Function of d_o

[31] It is well known that bedforms, and thus k_B, vary with wave conditions and grain size, but until recently, temporal variation of k_B has been difficult to detect in the field. *Trembanis et al.* [2004] report an order-of-magnitude change in wave friction factor and k_B between storm conditions and small waves, as well as significant variability in k_B between two sites with different grain sizes, separated by 1 km. *Styles and Glenn* [2002] also observed temporal variability in k_B. For orbital ripples, they found that k_B could be estimated as a constant times η. Both η and k_B varied by a factor of 2. In this experiment we observed even greater variability in k_B: Changes of 3 orders of magnitude occurred numerous times during the 2-month deployment. The range of k_B is large despite the fact that bedforms were relatively small, ranging from suborbital ripples to flat bed.

[32] The observed range of temporal variability in k_B suggests that the common use of constant k_B in numerical models of the wave-current boundary layer and of sediment transport is a significant source of error. One of our goals in estimating k_B was to determine the appropriate model input values for calculation of bottom shear stress. The $\hat{k}_B$ are too noisy to use as model input, and the requirements for calculating $\hat{k}_B$ ($R^2 \geq 0.96$, burst mean speed greater than 5 cm/s, and convergence of the inverse method) were not met for all bursts. Therefore we used the observed dependence of $\hat{k}_B$ on wave orbital diameter to develop a predictive equation for k_B. The 595 bursts for which $\hat{k}_B$ was calculated were divided into six groups based on the magnitude of d_o. A plot of the geometric means of $\hat{k}_B$

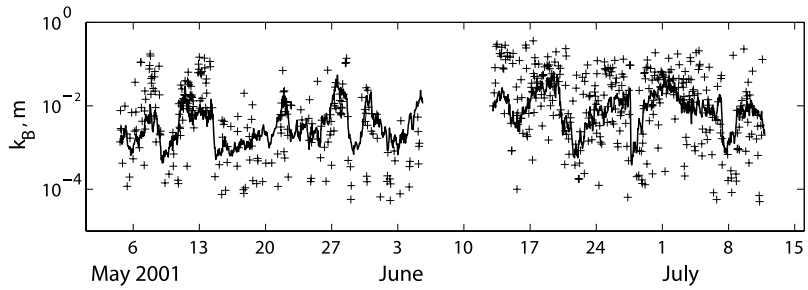

Figure 12. Bottom roughness $\hat{k}_B$ estimated for individual bursts (dots) and time series of predicted k_{Bpred} calculated from log linear relationship between wave orbital diameter and $\hat{k}_B$.

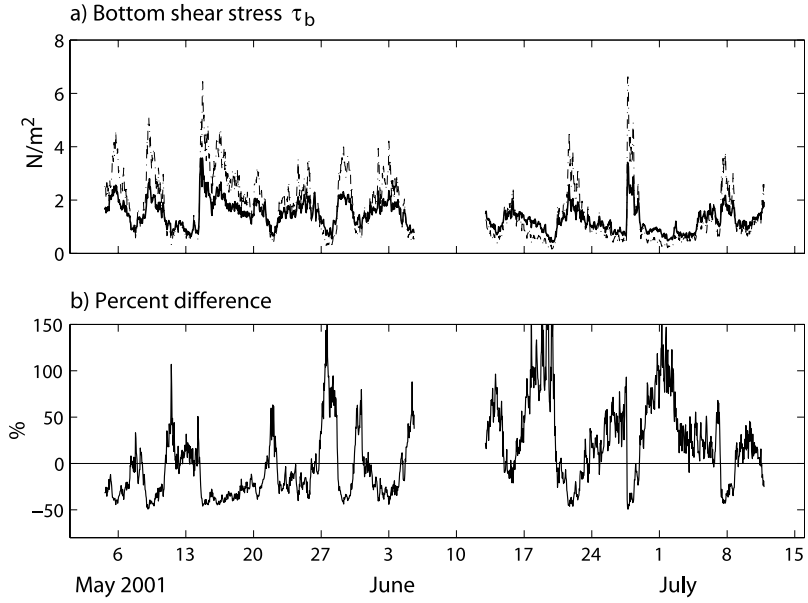

Figure 13. (a) Bottom shear stress τ_b calculated by GM with time-varying k_B (solid line) and with k_B = 0.5 cm (dash-dotted line). (b) Percent difference between τ_b calculated with time-varying and constant k_B.

versus d_o shows a logarithmic relationship between the two parameters (Figure 11), with a least squares fit line (R^2 = 0.989, 90% confidence interval on the slope of ±0.116) of

$$k_{\mathrm{Bpred}} = \exp[-5.4 - 2.3\ln(d_o)], \quad (5)$$

where the units of k_{Bpred} and d_o are meters. The time series of k_{Bpred} calculated from equation (5) preserves the low-frequency temporal variability apparent in the $\hat{k}_B$ values, but has a narrower range and is less noisy (Figure 12). It provides an estimate of bottom roughness for every burst, because k_{Bpred} depends only on d_o.

[33] To illustrate the importance of the observed variation in k_B to sediment transport, bottom shear stress τ_b was calculated with GM using the time series of k_{Bpred} (Figure 13). The resulting τ_b are at times 150% higher, and at times 50% lower, than those calculated from a constant k_B of 0.5 cm (the geometric mean of k_{Bpred}). Use of the geometric mean of k_{Bpred} overpredicts τ_b when waves are large and form drag is reduced by the absence of bedforms, and underpredicts τ_b when waves are smaller and larger bedforms increase form drag. These results show that it is critical to account for the time-varying nature of k_B in predicting τ_b and resuspension.

[34] It is important to note that equation (5) is specific to the conditions at our site. For this data set, k_B decreases with increasing wave energy, because the small grain size and the relatively energetic wave conditions produce ripples with heights that decrease with increasing wave height. Our method of estimating k_B can be applied to any data set, but the resulting relationship between $\hat{k}_B$ and d_o will depend on grain size, wave conditions, and the ratio of bottom orbital velocity to currents, and may not be log linear. In addition, any method for predicting k_B as a function of d_o alone cannot account for hysteresis in the relationship between wave energy and bedforms.

5.2. Comparison of Ripple Heights Estimated From $\hat{k}_B$ With Ripple Models

[35] Bedforms, when present, are the dominant influence on bottom roughness, and a number of methods have been proposed relating ripple height to k_B. To assess the reasonableness of the roughness estimates, we estimated bedform heights from the $\hat{k}_B$ and compared them with predicted and observed ripple heights.

[36] Ripples have been categorized into three types based on wave energy and grain size: orbital, which occur when the ratio of wave orbital diameter to grain size is low; anorbital, which occur when this ratio is high; and suborbital, which occur during the transition from orbital to anorbital [*Clifton and Dingler*, 1984; *Wiberg and Harris*, 1994]. The relationship between ripple height and k_B varies between these categories. The ratio d_o/D_{85} shows that conditions throughout the deployment were too energetic for orbital ripples, based on the points of transition between ripple categories identified by *Wiberg and Harris* [1994] (Figure 14).

[37] Orbital ripples have wavelength proportional to the orbital diameter ($\lambda = 0.65 d_o$) and a constant steepness $\eta/\lambda = 0.17$ [*Nielsen*, 1981; *Wiberg and Harris*, 1994]. For anorbital ripples, wavelength is a function of median grain size D, is independent of d_o, and can be estimated as $\lambda = 535D$. Anorbital ripples have a steepness η/λ no greater than 0.12; ripple height and steepness decrease with increasing wave energy. For the grain size at the study site, predicted anorbital wavelength is 9 cm and anorbital ripple height η should not exceed 1.08 cm, based on the equations from *Wiberg and Harris* [1994].

[38] Ripple height η was estimated from $\hat{k}_B$ based on the relationship between ripple height, steepness, and bedform

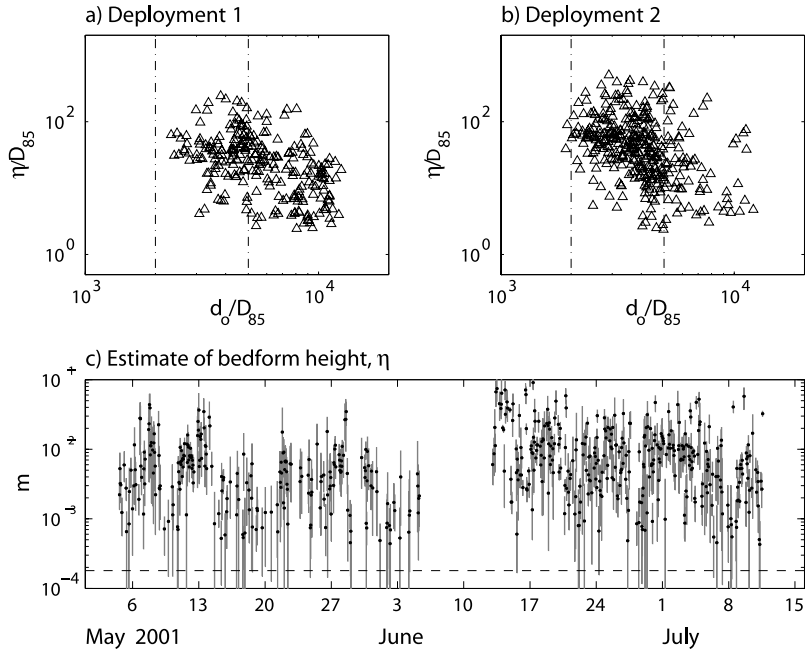

Figure 14. Estimated bedform height versus orbital diameter, both scaled by grain size, for (a) deployment 1 and (b) deployment 2. Dash-dotted lines show transition from orbital to suborbital (at $d_o/D = 2000$) and suborbital to anorbital (at $d_o/D = 5000$). (c) Bedform height estimated from equation (7). Dashed line is at D_{85}.

bottom roughness k_{BF} proposed by *Grant and Madsen* [1982],

$$k_{BF} = 27.7\,\eta\,\frac{\eta}{\lambda}. \tag{6}$$

We assume $k_{BF} = \hat{k}_B$, neglecting the contribution of grain roughness and saltating sediment. In applying equation (6), we assume a constant steepness of 0.15 for suborbital or orbital ripples and a constant wavelength $\lambda = 0.1$ m for anorbital ripples. Ripples with predicted height $\hat{\eta}$ less than 1 cm ($\hat{k}_B < 0.04$ m) are treated as anorbital. The resulting expression for ripple height is

$$\begin{aligned} \hat{\eta}_{ano} &= \sqrt{0.0036\,\hat{k}_B} \quad \hat{k}_B \le 0.04 \text{ m} \\ \hat{\eta}_{sub} &= \hat{k}_B/4 \qquad\quad \hat{k}_B > 0.04 \text{ m}. \end{aligned} \tag{7}$$

In developing this equation, we could have relied on a number of other proposed relationships and constants relating ripple height to bedform roughness. Our intention is not to propose a new method for estimating ripple height, nor to test existing methods. Our goal is to estimate the ripple heights corresponding to our hydrodynamically derived $\hat{k}_B$, so that we can compare them to predictions of ripple heights based on empirical relationships. The time series of $\hat{\eta}$ obtained from equation (7) shows that $\hat{\eta}$, like $\hat{k}_B$, is inversely related to wave energy (Figure 14). The error bars on $\hat{\eta}$ in Figure 14c are based on the uncertainty in $\hat{k}_B$.

[39] The $\hat{\eta}$ estimates are compared to predictions of ripple height based on *Nielsen* [1981], *Wiberg and Harris* [1994], and *Styles and Glenn* [2002] in Figure 15. All three predictive relationships are derived from analysis of field and laboratory data. *Nielsen* [1981] derived expressions for the ratio of ripple height to wave semi-excursion $A = d_o/2$ that are a function of the mobility number $\psi = (A\omega)^2/(s-1)g\,D$ alone, where ω is the angular frequency. He developed equations for field and laboratory data, and recommends use of the field equation for $\psi > 10$,

$$\frac{\eta}{A} = \begin{cases} 21\psi^{-1.85} & \psi > 10 \\ 0.275 - 0.022\sqrt{\psi} & \psi \le 10 \end{cases} \tag{8}$$

In this experiment, 4.2% of the bursts have $\psi < 10$.

[40] *Wiberg and Harris* [1994] (hereinafter referred to as WH) found that ripple steepness is strongly related to d_o/η, which serves as an estimate of the ratio of wave boundary-layer thickness to ripple height. For $d_o/\eta > 10$,

$$\frac{\eta}{\lambda} = \exp\left[-0.095\left(\ln\frac{d_o}{\eta}\right)^2 + 0.442\ln\frac{d_o}{\eta} - 2.28\right], \tag{9}$$

which can be solved iteratively for η, using $\lambda = 535D$. For $d_o/\eta \le 10$ (orbital ripples), ripple height is estimated from $\eta/\lambda = 0.17$ and $\lambda = 0.62$.

[41] *Styles and Glenn* [2002] (hereinafter referred to as SG) recalibrated the relationships for predicting η and λ developed by *Wikramanayake and Madsen* [1991] by including the data used by WH and the data of *Traykovski et al.* [1999], producing

$$\frac{\eta}{A} = \begin{cases} 0.30\left(\psi/S_*\right)^{-0.39} & \psi/S_* < 2 \\ 0.45\left(\psi/S_*\right)^{-0.99} & \psi/S_* \ge 2, \end{cases} \tag{10}$$

where $S_* = (D/4\nu)\sqrt{(s-1)gD}$ and ν is the kinematic viscosity of water. For our data, ψ/S_* is greater than 2 for all except one burst with $\psi/S_* = 1.97$.

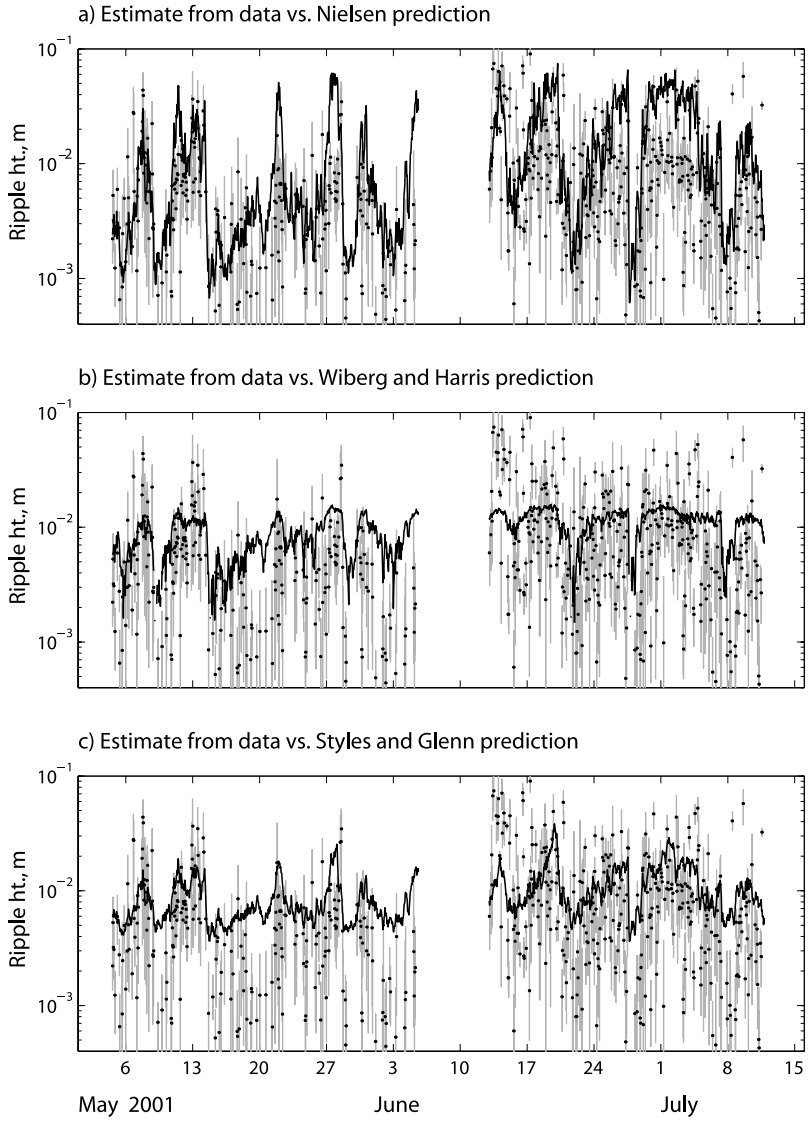

Figure 15. Ripple height estimated from data (dots) compared to predictions based on (a) *Nielsen* [1981], (b) *Wiberg and Harris* [1994], and (c) *Styles and Glenn* [2002].

[42] The temporal behavior of $\hat{\eta}$ is consistent with all three models: Bedforms were larger, on average, during the second than the first deployment, larger bedforms occurred during periods of low wave energy (12–15 May, 17–21 June, 29 June to 3 July), and bedforms were minimal during periods of highest wave energy (9 May, 15–17 May, 21 June, 28 June). In equations (8) and (10), ripple height depends on wave period (through ψ), so these models produce more variable predictions of ripple height than does the Wiberg and Harris model (equation (9)). The Nielsen equations predict much larger bedform heights than either our calculated $\hat{\eta}$ or those of the other two models under conditions classified as suborbital. The small ripple heights predicted by equation (8) when waves are large (9 May, 15–17 May, 21 June, 28 June) are more consistent with the $\hat{\eta}$ than the other two predictions.

[43] The response of $\hat{\eta}$ and the three predictors of ripple height (equations (8)–(10)) to d_o are illustrated in Figure 16. The $\hat{\eta}$ are consistent with other predictions of bedform heights both in range and in response to d_o, but are somewhat smaller. As in Figure 15, *Nielsen*'s [1992] predictions are consistent with $\hat{\eta}$ for large d_o but much larger than $\hat{\eta}$ for small d_o.

[44] In Figure 16, a grain size of 180 μ was used for all methods. In the *Nielsen* [1992] and SG formulae a constant wave period $T = 10$ s was assumed, which reduces the range of predicted ripple heights. The relationship between predicted ripple height and d_o for our data was determined by calculating ripple height from the log linear relationship between k_B and d_o (equation (5)) using equation (7). The dash-dotted line in Figure 16 shows the result of using a constant of 8 rather than 27.7 in equation (6), as recommended by *Nielsen* [1992]. This estimate is closer in magnitude to the predictions based on WH and SG.

[45] The dashed black line in Figure 16 shows the potential effect of saltating sediment on our estimates of ripple height. Roughness due to saltating sediment k_{ST} was estimated using the *Wiberg and Rubin* [1989] formulation. The k_{BF} was estimated as $k_B - k_{ST}$, the log linear relationship between the geometric means of k_{BF} and d_o was determined by linear

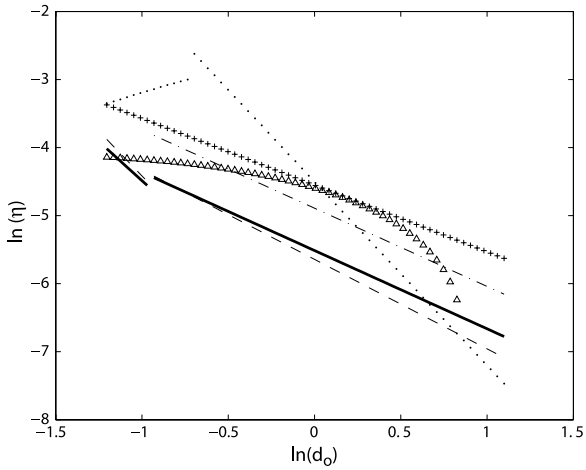

Figure 16. Relationship between predicted ripple height and wave orbital diameter based on equations (5) and (7) (solid line). Dashed line represents potential influence of saltating sediment on estimated bedform height, and dash-dotted line is predicted ripple height using a constant of 8 rather than 27.7 in equation (7). Models of *Nielsen* [1981] (dots), *Wiberg and Harris* [1994] (triangles), and *Styles and Glenn* [2002] (pluses) are shown as a function of d_o, assuming $D = 0.18$ mm and $T = 10$ s.

regression (as for equation (5)), and then equation (7) was applied. The dashed line represents an overestimate of the influence of saltating sediment, because k_{ST} was calculated using total bed shear stress τ_b rather than skin friction shear stress. Nevertheless, the influence is small, increasing only for large d_o, as $\hat{k}_B$ approaches 1 mm. In this range the contribution of grain roughness to k_B is significant as well, and the size of the predicted bedforms is minimal (<2 mm).

5.3. Comparison of $\hat{k}_B$ and $\hat{\eta}$ With Sonar Images

[46] Comparisons between the roughness estimates and the sonar results are limited because sonar data were recorded for less than half of the deployment and ripple heights were too small to resolve in the sonar images. Nevertheless, the sonar results provide an important qualitative comparison with $\hat{k}_B$ and $\hat{\eta}$. They confirm that the ripples present during the study were small in scale, that the types of bedforms present evolved over time (Figure 9), and that flat bed occurred during the most energetic waves. The average ripple wavelength in the plan view images (9.4 cm) is consistent with the predicted anorbital wavelength for the local grain size, suggesting that ripples were mostly anorbital. The maximum predicted height for anorbital ripples at this site is approximately 1 cm.

[47] From the sonar images we assigned one of the four bedform categories to each time interval, and to the associated $\hat{k}_B$, during the periods when the sonar was recording. We then computed the average $\hat{k}_B$ and $\hat{\eta}$ for each category. There were 188 instances of simultaneous estimates of bottom roughness and bedform category from sonar images, and the sample sizes for flat bed and linear ripples were quite limited. Mean $\hat{k}_B$ and $\hat{\eta}$ decreased with ripple type (ordered by increasing wave energy) (Figure 17). The mean bottom roughnesses at times of megaripples and flat bed are significantly smaller than at times of linear and irregular ripples, based on the 95% confidence interval on the mean. The long black error bars in Figure 17 (± standard deviation on the mean) overlap considerably, indicating that $\hat{k}_B$ (and $\hat{\eta}$) varied a great deal within each ripple type.

[48] Although megaripples are the largest bedform type, hydrodynamic roughness was lower for megaripples than for linear or irregular ripples. As a result, our method of estimating $\hat{\eta}$ does not detect megaripples. The observed megaripples typically had $\lambda > 1.5$ m and $\eta \sim 0.1-0.15$ m (Figure 10, especially 17–21 May). *Trembanis et al.* [2004] also found a decrease in roughness for large bedforms: The drag coefficient and wave friction factor were lower for a hummocky bed than when ripples were present. The authors attribute the reduction in drag to the smooth surface and low relief of the hummocks.

[49] The flow conditions producing megaripples in combined wave-current flows are not well understood and, as illustrated by Figure 15, available ripple models do not account for megaripples [*Li and Amos*, 1999]. *Li and Amos* [1999] suggest that megaripples form during periods of decreasing energy after storms and do not persist when currents are strong. On the other hand, *Gallagher et al.* [2003] found that there is no strong relationship between flow conditions and the occurrence of large bedforms in the surf zone.

6. Conclusions

[50] Estimated bottom roughness $\hat{k}_B$ ranged over 3 orders of magnitude (10^{-4} to 10^{-1} m) on the inner shelf of

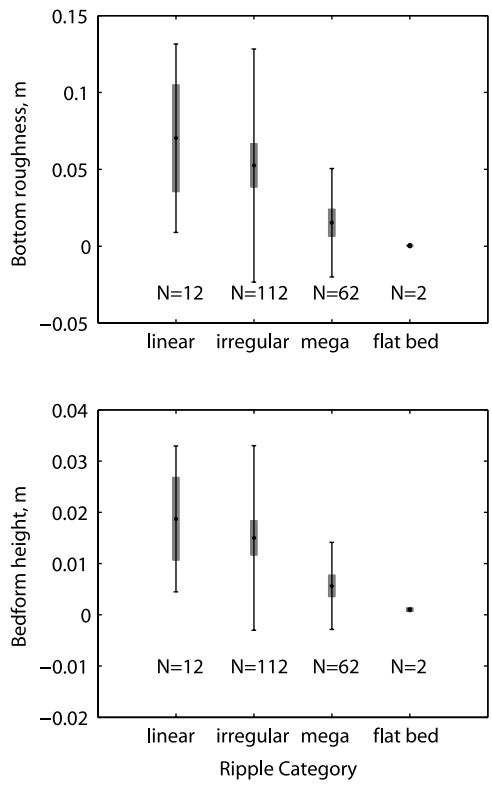

Figure 17. Bottom roughness $\hat{k}_B$ and bedform height $\hat{\eta}$ versus ripple category. Long error bars are ±1 standard deviation, and short error bars show the 95% confidence interval on the mean.

southwest Washington during 2 months in summer. The $\hat{k}_B$ was estimated from velocity profiles measured with a PCADP in the bottom boundary layer and inverse application of the GM model. The $\hat{k}_B$ varied inversely with wave energy, consistent with the expected relationship between k_B and d_o for the observed range of wave energies and grain size. Bottom roughness has not previously been estimated from hydrodynamic measurements for conditions as energetic as in this study, where bedforms were predominantly suborbital and anorbital ripples and flat bed. The PCADP provided velocity measurements at a greater number of heights in the bottom boundary layer than is practical with individual current meters, so that bottom roughness could be estimated for many points in time, encompassing a wide range of wave-current combinations.

[51] Variation in k_B over the observed range significantly influences predictions of sediment transport. Bed shear stress τ_b calculated with GM and a time-varying k_B (based on log linear regression between the estimated $\hat{k}_B$ and d_0) differed by up to 100% from τ_b calculated using a constant k_B. Models of hydrodynamics, resuspension, and sediment transport commonly use constant values for bottom roughness.

[52] Bedform height $\hat{\eta}$ (estimated from $\hat{k}_B$) decreased with increasing orbital diameter and compared well to ripple heights predicted by empirical ripple models. Sonar images showed that ripples, when present, were small in magnitude. The sonar images also showed that large bedforms ($\lambda \sim 1.5$ m), which were not reflected in the $\hat{\eta}$ or predicted by the ripple models, developed when significant wave height reached approximately 1.5 m. The large bedforms were particularly well developed during a period of decreasing wave energy. The large bedforms were not apparent in the $\hat{\eta}$ because the estimated bottom roughness $\hat{k}_B$ was lower on average for megaripples than for rippled beds.

[53] **Acknowledgments.** We thank Laura Kerr Landerman, Keith Kurrus, and Kevin Redman for help with data collection. This manuscript was significantly improved by suggestions from Pat Wiberg, Dan Hanes, and three anonymous reviewers. This study is part of the Southwest Washington Coastal Erosion Study, a joint project of the U.S. Geological Survey and the Washington Department of Ecology which is funded by the U.S. Geological Survey. Any use of trade, product, or firm names in this paper is for descriptive purposes only and does not imply endorsement by the U.S. Government.

References

Cacchione, D. A., and D. E. Drake (1990), Shelf sediment transport: An overview with applications to the northern California continental shelf, in *The Sea*, vol. 9, edited by B. LeMehaute and D. M. Hanes, chap. 21, pp. 729–773, John Wiley, Hoboken, N. J.

Clifton, H. E. (1976), Wave-formed sedimentary structures—A conceptual model, in *Beach and Nearshore Sedimentation*, edited by R. A. Davis and R. L. Ethington, pp. 126–148, Soc. of Econ. Paleontol. and Mineral., Tulsa, Okla.

Clifton, H. E., and J. R. Dingler (1984), Wave-formed structures and paleoenvironmental reconstruction, *Mar. Geol.*, *60*, 165–198.

Gallagher, E. L., E. B. Thornton, and T. P. Stanton (2003), Sand bed roughness in the nearshore, *J. Geophys. Res.*, *108*(C2), 3039, doi:10.1029/2001JC001081.

Glenn, S. M., and W. D. Grant (1987), A suspended sediment stratification correction for combined wave and current flows, *J. Geophys. Res.*, *92*(C8), 8244–8264.

Grant, W. D., and O. S. Madsen (1979), Combined wave and current interaction with a rough bottom, *J. Geophys. Res.*, *84*(C4), 1797–1808.

Grant, W. D., and O. S. Madsen (1982), Movable bed roughness in unsteady oscillatory flow, *J. Geophys. Res.*, *87*(C1), 469–481.

Grant, W. D., and O. S. Madsen (1986), The continental shelf bottom boundary layer, *Annu. Rev. Fluid Mech.*, *18*, 265–305.

Gross, T. F., and A. R. M. Nowell (1983), Mean flow and turbulence scaling in a tidal boundary layer, *Cont. Shelf Res.*, *2*, 109–126.

Hay, A. E., and D. J. Wilson (1994), Rotary side-scan images of near-shore bedform evolution during a storm, *Mar. Geol.*, *119*, 57–65.

Jonsson, I. G. (1966), Wave boundary layers and friction factors, in paper presented at 10th International Conference on Coastal Engineering, Am. Soc. of Civ. Eng., Reston, Va.

Lacy, J., and C. Sherwood (2004), Accuracy of a pulse-coherent acoustic Doppler profiler in a wave dominated environment, *J. Atmos. Oceanic Technol.*, *21*(9), 1448–1461.

Landerman, L. A., C. R. Sherwood, G. Gelfenbaum, J. Lacy, P. Ruggiero, D. Wilson, T. Chisholm, and K. Kurrus (2005), Grays Harbor sediment transport experiment: Spring 2001, *Data Ser. Rep. 98*, U.S. Geol. Surv., Washington, D. C.

Li, M. Z., and C. L. Amos (1998), Predicting ripple geometry and bed roughness under combined waves and currents in a continental shelf environment, *Cont. Shelf Res.*, *18*, 941–970.

Li, M. Z., and C. L. Amos (1999), Sheet flow and large wave ripples under combined waves and currents: Field observations, model predictions and effects on boundary layer dynamics, *Cont. Shelf Res.*, *19*, 637–663.

Madsen, O. S. (1994), Spectral wave-current bottom boundary layer flows, paper presented at 24th International Conference on Coastal Engineering, Am. Soc. of Civ. Eng., Reston, Va.

Madsen, O. S., L. D. Wright, J. D. Boon, and T. A. Chisholm (1993), Wind stress, bed roughness and sediment suspension on the inner shelf during an extreme storm event, *Cont. Shelf Res.*, *13*, 1303–1324.

Nielsen, P. (1981), Dynamics and geometry of wave-generated ripples, *J. Geophys. Res.*, *86*, 6467–6472.

Nielsen, P. (1992), *Coastal Bottom Boundary Layers and Sediment Transport*, World Sci., Hackensack, N. J.

Smith, J. D. (1977), Modeling of sediment transport on continental shelves, in *The Sea*, vol. 6, edited by E. D. Goldberg et al., pp. 539–577, John Wiley, Hoboken, N. J.

Soulsby, R. L., L. Hamm, G. Klopman, D. Myrhaug, R. R. Simons, and G. P. Thomas (1993), Wave-current interaction within and outside the bottom boundary layer, *Coastal Eng.*, *21*, 41–69.

Styles, R., and S. M. Glenn (2000), Modeling stratified wave and current bottom boundary layers on the continental shelf, *J. Geophys. Res.*, *105*(C10), 24,119–24,139.

Styles, R., and S. M. Glenn (2002), Modeling bottom roughness in the presence of wave-generated ripples, *J. Geophys. Res.*, *107*(C8), 3110, doi:10.1029/2001JC000864.

Traykovski, P., A. E. Hay, J. D. Irish, and J. E. Lynch (1999), Geometry, migration, and evolution of wave orbital ripples at LEO-15, *J. Geophys. Res.*, *104*(C1), 1505–1524.

Trembanis, A., L. Wright, C. Friedrichs, M. Green, and T. Hume (2004), The effects of spatially complex inner shelf roughness on boundary layer turbulence and current and wave friction: Tairua embayment, New Zealand, *Cont. Shelf Res.*, *24*, 1549–1571.

Wiberg, P. L., and C. K. Harris (1994), Ripple geometry in wave-dominated environments, *J. Geophys. Res.*, *99*, 775–789.

Wiberg, P. L., and D. M. Rubin (1989), Bed roughness produced by saltating sediment, *J. Geophys. Res.*, *94*(C4), 5011–5016.

Wiberg, P. L., D. E. Drake, and D. A. Cacchione (1994), Sediment resuspension and bed armoring during high bottom stress events on the northern California inner continental shelf: Measurements and predictions, *Cont. Shelf Res.*, *14*, 1191–1219.

Wikramanayake, P. N., and O. S. Madsen (1991), Calculation of movable bed friction factors, *Tech. Prog. Rep. DACW-39-88-K-0047*, 105 pp., U.S. Army Corps of Eng., Vicksburg, Miss.

Xu, J. P., and L. D. Wright (1995), Test of bed roughness models using field data from the Middle Atlantic Bight, *Cont. Shelf Res.*, *15*, 1409–1434.

T. A. Chisholm, Department of Environmental Science and Engineering, Oregon Graduate Institute, 20000 NW Walker Road, Beaverton, OR 97006, USA. (chisholm@ese.ogi.edu)

G. R. Gelfenbaum, U.S. Geological Survey, Coastal and Marine Geology, 345 Middlefield Road, MS-999, Menlo Park, CA 94025, USA. (ggelfenbaum@usgs.gov)

J. R. Lacy, U.S. Geological Survey, Coastal and Marine Geology, 400 Natural Bridges Drive, Santa Cruz, CA 94060, USA. (jlacy@usgs.gov)

C. R. Sherwood, U.S. Geological Survey, Coastal and Marine Geology, 384 Woods Hole Road, Woods Hole, MA 02543, USA. (csherwood@usgs.gov)

D. J. Wilson, Imagenex Technology Corporation, 209–1875 Broadway Street, Port Coquitlam, BC, V3C 4Z1 Canada. (dougw@ese.ogi.edu)